JOURNAL OF GEOPHYSICAL RESEARCH, VOL. 113, D08209, doi:10.1029/2007JD009257, 2008



# Effects of aerosol optical properties on deep convective clouds and radiative forcing

Jiwen Fan,[1,4] Renyi Zhang,[1] Wei-Kuo Tao,[2] and Karen I. Mohr[3]

Received 6 August 2007; revised 26 November 2007; accepted 19 December 2007; published 23 April 2008.

[1] The aerosol radiative effects (ARE) on the deep convective clouds are investigated by using a spectral-bin cloud-resolving model coupled with a radiation scheme and an explicit land surface model. The sensitivity of cloud properties and the associated radiative forcing to aerosol single-scattering albedo (SSA) are examined. The ARE on cloud properties is pronounced for mid-visible SSA of 0.85. Relative to the case without ARE, the cloud fraction and optical depth decrease by about 18% and 20%, respectively. Ice particle number concentrations, liquid water path, ice water path, and droplet size decrease by more than 15% when the ARE is introduced. The ARE causes a surface cooling of about 0.35 K and significantly high heating rates in the lower troposphere (about 0.6 K day$^{-1}$ higher at 2 km), both of which lead to a more stable atmosphere and hence weaker convection. The weaker convection explains the less cloudiness, lower cloud optical depth, less LWP and IWP, smaller droplet size, and less precipitation resulting from the ARE. The daytime-mean direct forcing induced by black carbon is about 2.2 W m$^{-2}$ at the top of atmosphere (TOA) and $-17.4$ W m$^{-2}$ at the surface for SSA of 0.85. The semi-direct forcing is positive, about 10 and 11.2 W m$^{-2}$ at the TOA and surface, respectively. Both the TOA and surface total radiative forcing values are strongly negative for the deep convective clouds, attributed mostly to aerosol indirect forcing. Aerosol direct and semi-direct effects are very sensitive to SSA when aerosol optical depth is high. Because the positive semi-direct forcing compensates the negative direct forcing at the surface, the surface temperature and heat fluxes decrease less significantly with the increase of aerosol absorption (decreasing SSA). The cloud fraction, optical depth, convective strength, and precipitation decrease with the increase of absorption, resulting from a more stable atmosphere due to enhanced surface cooling and atmospheric heating.

**Citation:** Fan, J., R. Zhang, W.-K. Tao, and K. I. Mohr (2008), Effects of aerosol optical properties on deep convective clouds and radiative forcing, *J. Geophys. Res.*, *113*, D08209, doi:10.1029/2007JD009257.

## 1. Introduction

[2] Aerosols interact directly and indirectly with the Earth's radiation budget and climate. As for the direct effect, aerosols scatter and absorb solar radiation [*Charlson and Pilat*, 1969; *Coakley et al.*, 1983]. As for the indirect effect, aerosols act as cloud condensation nuclei (CCN) and affect cloud properties [*Twomey*, 1977; *Rosenfeld*, 2000]. Also, aerosol absorption and backscattering modify the atmospheric temperature structure, decreases the solar radiation at the surface, and lowers surface moisture fluxes, suppressing convection and reducing cloud fraction [*Ackerman et al.*, 2000; *Ramanathan et al.*, 2001b]. This phenomenon has been referred as to the "semi-direct effect" [*Hansen et al.*, 1997; *Johnson et al.*, 2004]. The addition of anthropogenic aerosols to the atmosphere may change the radiative fluxes at the top-of-atmosphere (TOA), at the surface, and within the atmospheric column. Recent reports summarize that on a global average the sum of direct and indirect forcing by anthropogenic aerosols at the TOA is likely to be negative and may be comparable in magnitude to the positive forcing of about 2.4 W m$^{-2}$ by anthropogenic greenhouse gases [*Intergovernmental Panel on Climate Change (IPCC)*, 2001]. Large uncertainties exist in current estimates of the aerosol forcing because of incomplete knowledge concerning the distribution and the physical and chemical properties of aerosols as well as aerosol-cloud interactions.

[3] The estimation of the direct radiative forcing exerted by aerosol is complex to quantify because anthropogenic particles are generally a complex mixture of different chemical components [*Hegg et al.*, 1997; *Ramanathan et al.*, 2001a; *Levitt et al.*, 2007]. The uncertainty of the

[1]Department of Atmospheric Sciences, Texas A&M University, College Station, Texas, USA.
[2]NASA Goddard Space Flight Center, Greenbelt, Maryland, USA.
[3]Department of Earth and Atmospheric Sciences, University at Albany, SUNY, Albany, New York, USA.
[4]Now at Climate Physics, Pacific Northwest National Laboratory, Richland, Washington, USA.


0148-0227/08/2007JD009257$09.00

aerosol direct climate forcing is about a factor of 2 to 3, whereas the indirect forcing is even much larger and difficult to quantify [*IPCC*, 2001]. The measured TOA direct forcing on the regional scale ranges from −9 to 2 W m$^{-2}$ [*Ramanathan et al.*, 2001b; *Ramachandran*, 2005]. The semi-direct effect introduces added feedbacks due to the radiative properties of the aerosol (i.e., absorption), and has been studied in the recent years. *Ackerman et al.* [2000] showed that a decrease in cloudiness commensurate with heating associated with absorbing aerosols. *Johnson et al.* [2004] and *Feingold et al.* [2005] suggested the importance of the vertical location of the absorbing aerosol: Absorbing aerosol may reduce or increase the cloud water and cloud fraction. On the other hand, the reduction in downwelling solar radiation and associated decrease in surface latent and sensible heat fluxes result in significant reduction in cloud water and cloud fraction [*Feingold et al.*, 2005; *Jiang and Feingold*, 2006]. The semi-direct forcing was estimated to be about 15 W m$^{-2}$ for stratocumulus [*Johnson et al.*, 2004] and 7.5 W m$^{-2}$ for trade cumulus [*Ackerman et al.*, 2000].

[4] Black carbon (BC) is an important absorbing aerosol produced primarily from incomplete fossil fuel and biomass burning. In the atmosphere, BC particles interact with other aerosol particles and gas phase species and exist at various mixing states [*Zhang and Zhang*, 2005]. The impact of BC on clouds and radiative forcing depends on the mixing state. Coating on BC aerosols may significantly increase the absorption of solar radiation [*Chylek et al.*, 1995]. BC was commonly treated as a core coated by the other components when studying aerosol radiative properties [*Ackerman and Toon*, 1981; *Jacobson*, 1999]. It has been demonstrated that the climate effects of BC aerosols are more significant on the regional scale than on the global scale [*Wang*, 2004]. A polluted urban atmosphere typically has an elevated aerosol loading because of emissions from transportation and industry [*Zhang et al.*, 2004a], which may exert significant aerosol radiative forcing. High ozone and aerosol concentrations (over $10^5$ cm$^{-3}$) have been identified to exist in the Houston area, associated with transportation and industrial activities [*Brock et al.*, 2003; *Lei et al.*, 2004; *Zhang et al.*, 2004b; *Li et al.*, 2005, 2007; *Fan et al.*, 2006]. Evidence has been provided that high aerosol loading over Houston may considerably affect cloud development and even lightning activity [*Bond et al.*, 2001; *Orville et al.*, 2001; *Zhang et al.*, 2003]. The observed BC mass concentrations at LaPorte in Houston were up to 2.0 $\mu$g m$^{-3}$ [*Fast et al.*, 2006], and the simulated mass mixing ratio of BC to ammonium sulfate was up to 1:8 [*Fan et al.*, 2005]. The effect of anthropogenic aerosols on direct radiative forcing is significant in the vicinity and downwind of the urban area of Houston. The observed aerosol radiation forcing during the afternoon periods was between −30 and −80 W m$^{-2}$ [*Fast et al.*, 2006]. *Fast et al.* [2006] also indicated that the predicted shortwave radiation was 30 to 40 W m$^{-2}$ closer to the observations in the vicinity of Houston when the aerosol radiative properties were incorporated into the shortwave radiation scheme.

[5] We have previously investigated the aerosol indirect effect on the cumulus clouds in the Houston area using a two-dimensional cloud-resolving Goddard Cloud Ensemble (GCE) model with the spectral-bin cloud microphysics [*Fan et al.*, 2007a, 2007b]. In this paper, a more comprehensive investigation of aerosol effects on deep convective clouds is performed by incorporating the radiative transfer processes and the land-atmosphere interaction processes into the GCE model, focusing on the radiative effects of anthropogenic aerosols containing BC. An aerosol radiative module is developed to calculate the wavelength-dependent aerosol radiative properties based on the aerosol composition, size distribution, mixing state, and ambient relative humidity. The significance of the aerosol radiative effects (ARE) is investigated by comparing with the case excluding the ARE. The associated aerosol direct, semi-direct and indirect radiative forcing values for deep convective clouds are estimated, and the sensitivity of cloud properties and radiative forcing to aerosol single-scattering albedo (SSA) are examined. Although the effects of aerosols including absorbing components on clouds and radiative forcing have been investigated by model simulations in previous studies [*Johnson et al.*, 2004; *Feingold et al.*, 2005; *Jiang and Feingold*, 2006; *McFarquhar and Wang*, 2006], few studies have simultaneously examined the aerosol direct, semi-direct, and indirect effects on clouds using a spectral-bin cloud-resolving model (CRM) coupled with a state-of-the-art land surface model and an aerosol radiative module to online calculate the aerosol radiative properties.

## 2. Model Description

[6] The GCE model employed in the present study is 2-D and nonhydrostatic. The description of the model dynamics and microphysics has been presented by *Fan et al.* [2007a], and more details on those processes are discussed by *Khain et al.* [2004] and *Tao et al.* [2003a]. The 2-D spectral-bin cloud model employed in the present study has been extensively validated for its capability to capture the macro- and microphysical characteristics of deep convective clouds [*Fan et al.*, 2007a, 2007b; *Johnson et al.*, 2004; *Tao and Simpson*, 1993; *Khain and Pokrovsky*, 2004]. Several previous studies have also concluded that, although some aspects of 2-D simulations differ from 3-D simulations, many important statistical characteristics, such as mean temperature and water profile, cloud fraction, and precipitation rates, etc., tend to be similar [*Khairoutdinov and Randall*, 2003].

[7] The spectral-bin microphysics is based on solving an equation system for eight number size distributions for water drops, ice crystals (columnar, plate-like and dendrites), snowflakes, graupel, hail/frozen drops and aerosols/CCN. Each size distribution is represented by 33 mass doubling bins. The initial aerosol size distribution was originally calculated by an empirical formula: $N = N_0 S_w^k$ [*Pruppacher and Klett*, 1997], where $S_w$ is the supersaturation with respect to water, and the CCN activation is calculated for single-component aerosols according to the Köhler theory. We have modified the initial aerosol size distribution and CCN activation [*Fan et al.*, 2007a, 2007b], to reflect the aerosol/CCN characteristics in the Houston region. The activation schemes for multiple-component soluble aerosols and aerosols with a slightly soluble or insoluble core have been incorporated into the GCE model to investigate the effects of aerosol chemical compositions on clouds [*Fan et al.*, 2007a]. The supersaturations with respect to water and ice are calculated with an explicit analytical method. The

supersaturation ($S_w$) used to calculate droplet nucleation is linked to the droplet growth by diffusion.

[8] The GCE model employed in this study has been further updated by incorporating a Goddard radiation scheme and an explicit Goddard land surface model, Parameterization for Land-Atmosphere-Cloud Exchange (PLACE) [*Wetzel and Boone*, 1995; *Tao et al.*, 2003a], to investigate the aerosol radiative effects on deep convective clouds and the associated forcing. An aerosol radiative module has been developed and coupled into the radiation scheme to on-line calculate the wavelength-dependent aerosol optical depth (AOD), single-scattering albedo (SSA), and asymmetry factor (AF) based on the aerosol characteristics and ambient relative humidity.

### 2.1. PLACE Land Surface Model and Goddard Radiation Scheme

[9] The PLACE represents a detailed interactive process model of the heterogeneous land surface (soil and vegetation) and adjacent near-surface atmosphere. PLACE consists of linked process models (e.g., net radiation, evapotranspiration, ground heat storage) and emphasizes the vertical transport of moisture and energy through the 5 layer soil moisture and the 7 layer soil temperature column to the overlying heterogeneous land surface. The additional two soil temperature layers are used to aid in resolving large temperature gradients near the surface. Momentum, sensible, and latent heat fluxes are calculated using similarity relationships [*Zilitinkevich*, 1975; *Businger et al.*, 1971]. More details on the description of PLACE are presented by *Wetzel and Boone* [1995]. The atmospheric component of GCE provides surface winds, surface air temperature, surface pressure, moisture, shortwave and longwave radiation, and precipitation to the land surface model (PLACE). The land surface component returns momentum, sensible heat, and latent heat fluxes to the atmosphere, and the coupling is two-way interactive. A 2-D GCE coupled with the PLACE model has previously been utilized to investigate landscape-generated deep convection [*Lynn et al.*, 1998; *Baker et al.*, 2001] and the sensitivity of convection to land cover in the semi-arid regions of West Africa [*Mohr et al.*, 2003; *Alonge et al.*, 2007].

[10] The latest version of the Goddard radiation scheme includes shortwave and longwave radiation models [*Tao et al.*, 2003a, 2003b]. The shortwave radiation model of *Chou and Suarez* [1999] is employed to compute the solar fluxes due to absorption and scattering by clouds, aerosols and gases (including water vapor). Fluxes are integrated virtually over the entire spectrum, from 0.175 to 10 $\mu$m. The spectrum is divided into seven bands in the ultraviolet (UV) region (0.175–0.4 $\mu$m), one band in the photosynthetically active radiation (PAR) region (0.4–0.7 $\mu$m), and three bands in the near infrared region (0.7–10.0 $\mu$m). In the UV and PAR region, a single $O_3$ absorption coefficient and a Rayleigh scattering coefficient are used for each of the eight bands. In the infrared wavelength range, the *k*-distribution method is applied to compute the absorption of solar radiation. Reflection and transmission of a cloud and aerosol-laden layer are computed according to the $\delta$-Eddington approximation. Fluxes for a composite of layers are then computed using the two-stream adding approximation. The longwave radiation parameterizations developed by *Chou et al.* [1999] and *Kratz et al.* [1998] are implemented into the GCE model. The IR spectrum is divided into nine bands. In addition, a narrow band in the 17 $\mu$m region is added to compute flux reduction due to $N_2O$. In the solar spectral region, the *k*-distribution method with temperature and pressure scaling is used to compute the transmission function in the weak absorption bands of water vapor and minor trace gases ($N_2O$, $CH_4$, CFC's). A look-up table method is used to compute the transmission function in the strong absorption bands.

### 2.2. Aerosol Radiative Module

[11] The wavelength-dependent aerosol radiative properties such as AOD ($\tau$), SSA ($\sigma$), and AF ($g$) are the key factors to determine the aerosol radiative effects on clouds and associated forcing. Instead of using the fixed aerosol radiative properties during the simulations as in some previous studies [e.g., *Johnson et al.*, 2004; *McFarquhar and Wang*, 2006], an aerosol radiative module has been developed and incorporated into the radiation scheme to online calculate the aerosol radiative properties as a function of wavelength ($\lambda$), on the basis of the aerosol composition, size distribution, mixing state, and ambient relative humidity. The module includes the methodologies for the external and core-coated internal mixing states.

[12] For the internally mixed aerosol components, the complex refractive index of aerosol particles is calculated based on the volume-weighted average of the individual refractive index [*Hänel*, 1976]. The real and imaginary parts of the complex refractive index, denoted by $\overline{n}(i, \lambda)$ and $\overline{k}(i, \lambda)$, respectively, for aerosols in a size bin ($i$) at a certain wavelength ($\lambda$) are determined by:

$$\overline{n}(i,\lambda) = \sum_{l=1}^{m} n(l,i,\lambda) f(l), \overline{k}(i,\lambda) = \sum_{l=1}^{m} k(l,i,\lambda) f(l) \quad (1)$$

where $m$ is the number of aerosol components and $f(l)$ is the volume fraction of the component ($l$). The Mie theory [*Bohren and Huffman*, 1983] is employed to calculate the extinction efficiency ($Q_e$), scattering efficiency ($Q_s$), and asymmetry factor ($g$) as functions of the size parameter, $x = 2\pi r/\lambda$, where $r$ is the particle's wet radius. The hygroscopic growth of a water-soluble component at a certain ambient humidity is calculated by the relation defined by *Mallet et al.* [2004],

$$r_{g,a(o)} = r_{g,a(b)}(1-h)^e \quad (2)$$

where $h$ is the relative humidity. In general, aerosols over polluted urban area such as in Houston are a complex mixture of organic and inorganic components, whose composite hygroscopicity is difficult to quantify. Models and measurements have suggested about 30% sulfate and 32% organics (including elemental carbon (EC)) in the total $PM_{2.5}$ mass [*Fan et al.*, 2005]. The coefficient $e$ depends on the aerosol type, and is equal to 0.25 for particulate organic matter [*Chazette and Liousse*, 2001] and 0.285 for ammonium sulfate, nitrate, and sea salt [*Hänel*, 1976]. In the present study, a value of 0.25 for $e$ is employed for the internal mixture of ammonium sulfate and BC. Clearly, the applications of equation (2) and the exponent factor need to be validated by future field studies.

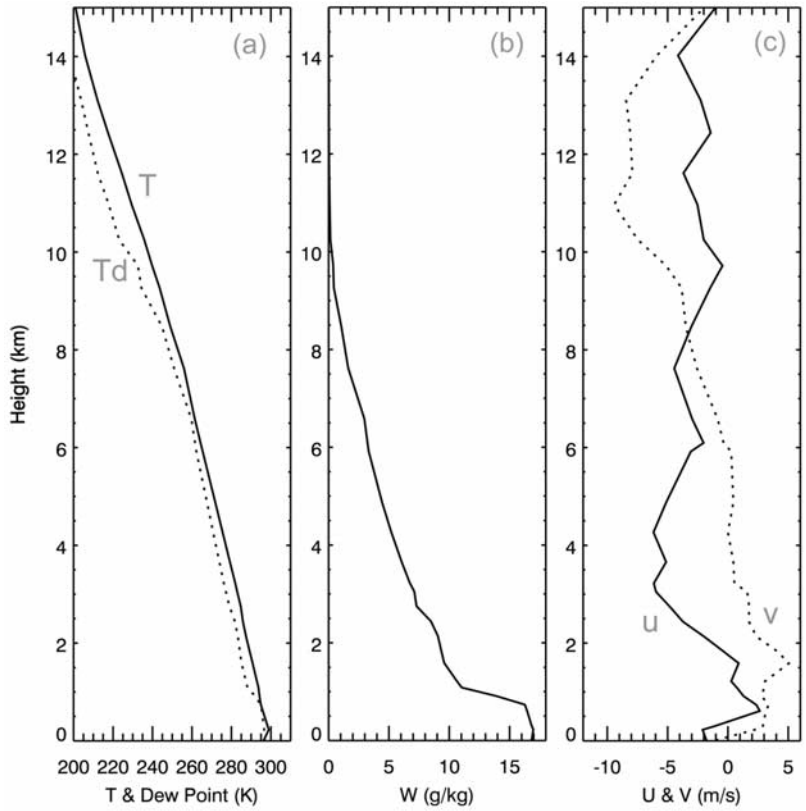


**Figure 1.** Initial profiles of temperature ($T$), dew point ($Td$), water vapor mixing ratio ($w$), and horizontal winds $u$ and $v$ from a sounding near Houston at 7:00 am on 24 August 2000.

[13] To avoid repeated Mie calculations at the later time steps, we first obtain a look-up table containing aerosol optical properties, i.e., $Q_e$, $\sigma$, and $g$, over all size ranges covered by 33 bins and a set of refractive indices that represent a range of indices typical of atmospheric aerosols by performing full Mie calculations. In all subsequent steps of this algorithm, the Mie calculations are skipped, and the $Q_e$, $\sigma$, and $g$ for an aerosol particle are obtained by interpolating linearly from the look-up table with the calculated complex refractive index and size parameter according to the aerosol characteristics and relative humidity.

[14] The aerosol optical depth ($\tau(\lambda, j)$) at a certain $\lambda$ and atmospheric layer ($j$) is calculated by integration over the aerosol particles in all of 33 size bins,

$$\tau(\lambda,\ j) = \sum_{i=1}^{33} Q_e(\lambda, r_i)\pi r_i^2 n(r_i, j)dz_j \tag{3}$$

where $n(r_i, j)$ represents the aerosol number concentrations and $dz_j$ is the height of the atmospheric layer. Note that $r_i$ is the wet particle radius corrected with the hygroscopic growth and calculated from equation (2). Assuming $\tau(\lambda, r_i, j) = Q_e(\lambda, r_i)\pi r_i^2 n(r_i, j)dz_j$, the weighted-mean values of SSA ($\sigma$) and AF ($g$) for the aerosol mixture at a certain wavelength and layer are calculated by

$$\sigma(\lambda,\ j) = \sum_{i=1}^{33} \tau(\lambda, r_i, j)\sigma(\lambda, r_i, j) \Big/ \sum_{i=1}^{33} \tau(\lambda, r_i, j) \tag{4}$$

$$g(\lambda,\ j) = \sum_{i=1}^{33} \tau(\lambda, r_i, j)\sigma(\lambda, r_i, j)g(\lambda, r_i, j) \Big/ \sum_{i=1}^{33} \tau(\lambda, r_i, j)\sigma(\lambda, r_i, j) \tag{5}$$

[15] For the externally mixed aerosol components, the aerosol radiative properties $\tau$, $\sigma$, and $g$ are first calculated for each component, and the ensemble aerosol radiative properties for the total aerosol population are summed over all of the components [*Wolf*, 2002].

[16] Once the wavelength-dependent aerosol radiative parameters $\tau$, $\sigma$, and $g$ are determined, they are transferred to the shortwave and longwave radiative transfer models and then interact with the other components of GCE such as dynamical, microphysical, and surface processes along with the cloud radiative properties.

## 3. Model Configuration and Validation

### 3.1. Initial Conditions and Design of Numerical Experiments

[17] The initial sounding used in the simulations is from Lake Charles (93.21W, 30.11N) near the Houston area, and is at 7:00 am (local time) on 24 August 2000 (Figure 1). The vertical temperature and dew point profiles reveal an unstable atmosphere with a convective available potential energy (CAPE) of 1800 J kg$^{-1}$, integrated from the level of 500 m. The surface temperature is 23.2°C and the surface relative humidity is 87% (Figures 1a and 1b). The sounding

**Table 1.** Selected Vegetation and Soil Characteristics Used in PLACE

| Vegetation: Broadleaf Bushes/Trees With Groundcover | | Soil: Sandy Clay Loam | |
|---|---|---|---|
| Albedo | 0.14 | Albedo | 0.15 |
| % Veg. cover | 30% | Porosity | 0.42 |
| Leaf area index | 4.0 | Saturated hydraulic conductivity | $6.1 \times 10^{-4}$ |
| Root profile | 0.00 | Initial soil moisture | 0.18–0.21 |
| layers 1–5 | 0.25 | layers 1–5 | 0.20–0.22 |
| | 0.50 | | 0.23–0.26 |
| | 0.20 | | 0.25–0.28 |
| | 0.05 | | 0.25–0.28 |
| Surface roughness | 1.0 | % Silt | 20% |
| Minimum stomatal resistance | 110.0 | % Sand | 55% |
| Biomass heat capacity | 5.0 | % Clay | 25% |

Legend: % veg. cover is the percentage of area covered by transpiring vegetation; root profile is the cumulative frequency distribution of roots in the 5 soil moisture reservoirs; surface roughness in m; minimum stomatal resistance is in s $m^{-1}$; surface biomass (water-equivalent) heat capacity in J $K^{-1}$ $m^{-2}$. For soil, saturated hydraulic conductivity in m $s^{-1}$. Initial soil moisture is expressed as volumetric ($cm^3$ $cm^{-3}$) soil moisture, the ratio of the volume of soil water to total soil volume.

also reveals a weak wind shear (Figure 1c). The computational domain is composed of 1024 × 33 grid points with a horizontal resolution of 500 m. There are 33 stretched vertical levels with a resolution of 280 m at the lowest level and 1260 m at the top. Open boundary conditions are used at the lateral boundaries. The dynamic time step is 6 s. The time steps for diffusion growth and droplet nucleation is several times smaller than the dynamic time step, which are chosen to be equal to the time required for particles in the smallest nonempty bin to reach the next mass category during condensation or to be transferred to a neighboring mass bin during evaporation [*Khain et al.*, 2004]. The radiation and land surface processes are calculated every 3 min.

[18] The initial surface conditions for PLACE are broadly representative of land cover in the Houston area as shown in Table 1. This heavily urbanized region contains a mixture of impervious cover, lawns, and deciduous broadleaf trees and bushes. The soils are typical of coastal plains, sandy and silty clays and clay loams. The low percentage of vegetation cover reflects the sprawling urban infrastructure of buildings and transportation networks. Initial soil moisture and soil temperature values are based on examination of the NCEP/NCAR daily reanalysis of soil moisture, soil temperature, and precipitation for the week preceding 24 August 2000. The reanalysis of volumetric soil moisture in the layers 0–10 cm and 10–200 cm for the Houston area has a range of 0.20–0.28 $cm^3$ $cm^{-3}$. The initial soil moisture values in Table 1 assume additional drying in the layers above 10 cm after rainfall on 22 August. Both soil temperature and moisture are randomly varied within the ranges in Table 1 across the model domain to account for the variability of the urban landscape.

[19] A series of sensitivity simulations have been performed. We first perform a control run, i.e., AR_85, considering aerosol radiative effects. The initial aerosol size distribution in AR_85 is from the modeled results and has been compared and validated with the observations [*Fan et al.*, 2006, 2007a, 2007b]. The aerosol concentration with the size larger than 60 nm is over 1000 $cm^{-3}$. Aerosols are represented by internal BC-cores surrounded by ammonium sulfate. Preliminary analysis from in situ measurements of the mixing states of BC during TexAQS 2006 shows about 70% internally mixed BC in the Houston area [*J. P. Schwarz* of NOAA, personal communication]. The mass mixing ratios are assumed to be about 0.1 for BC and 0.9 for ammonium sulfate (Table 2). The activation scheme accounting for the effect of the insoluble core is employed to calculate CCN activation [*Fan et al.*, 2007a]. As shown in Table 2, the mid-visible (at 0.55 $\mu$m) SSA in AR_85 is 0.85, and AOD and AF are 0.27 and 0.76, respectively, at the initial time of the simulation, calculated from the aerosol radiative module and consistent with observations in Houston. Generally, the observed mid-visible AOD is between 0.25 and 0.4, and the SSA falls in the range of 0.85–0.95. To isolate the aerosol radiative effects, an additional simulation referred to as NAR_00 is performed without considering ARE. Hence NAR _00 is similar to AR_85, except that the aerosol radiative properties, i.e., AOD, SSA, and AF, are set to zero (without the aerosol radiative module) (Table 2). Two additional simulations are performed for background aerosols (ammonium sulfate only), considering the aerosol radiative effects to estimate the values of aerosol radiative forcing, with one corresponding to the polluted aerosol case referred to as SA_100 and the other corresponding to the clean aerosol case as SAC_100. SA_100 has the same initial aerosol size distribution as AR_85, but a simple Köhler theory is employed for the activation of ammonium sulfate. SAC_100 has a similar configuration as SA_100, except that the aerosol concentration is only about 7% of SA_100, which is about 3000 $cm^{-3}$ (sum over the size distribution $dN/dln(D_p)$). As shown in Table 2, the SSA values for both cases are 1.0, since ammonium sulfate only has a scattering effect. The AOD at 0.55 nm is 0.25 for SA_100, but is 0.009 for SAC_100. For all of the simulations, an exponential decrease in aerosol concentrations with heights is used as the initial condition at $t = 0$: $N_0 = N_0(z = 0)\exp((z - z_0)/\Delta z)$, where $z_0 = 2.0$ km and $\Delta z = 1.2$ km, which are obtained from the CMAQ aerosol simulations [*Fan et al.*, 2007a, 2007b]. Aerosols are distributed uniformly below 2 km (assuming well-mixed).

[20] Additional simulations are performed on the sensitivity of aerosol radiative effects to SSA. The mass ratio of BC to ammonium sulfate is varied to yield the aerosol mixtures with a range of mid-visible SSA: 0.85, 0.9, 0.95, and 1.0 for pure ammonium sulfate. These reflect the typical range of mid-visible SSA values observed in the atmosphere. The calculations with the SSA of 0.85 and 1.0 correspond to the simulations of AR_85 and SA_100, respectively. The

**Table 2.** Aerosol Properties in Numerical Simulations

| Cases | Composition[a] | Conc., $cm^{-3}$ [b] | AOD[c] | SSA[c] | AF[c] |
|---|---|---|---|---|---|
| NAR_00 | 0.9 Ammo. Sulf. 0.1 BC | $4.2 \times 10^4$ | 0.0 | 0.0 | 0.0 |
| AR_85 | 0.9 Ammo. Sulf. 0.1 BC | $4.2 \times 10^4$ | 0.27 | 0.85 | 0.76 |
| SA_100 | 1.0 Ammo. Sulf. | $4.2 \times 10^4$ | 0.25 | 1.00 | 0.76 |
| SAC_100 | 1.0 Ammo. Sulf. | $3 \times 10^3$ | 0.009 | 1.00 | 0.72 |

[a] Based on mass mixing ratios.
[b] The concentration is the sum over the aerosol size distribution $dN/dln(D_p)$.
[c] Values shown are at the wavelength of 0.55 $\mu$m.

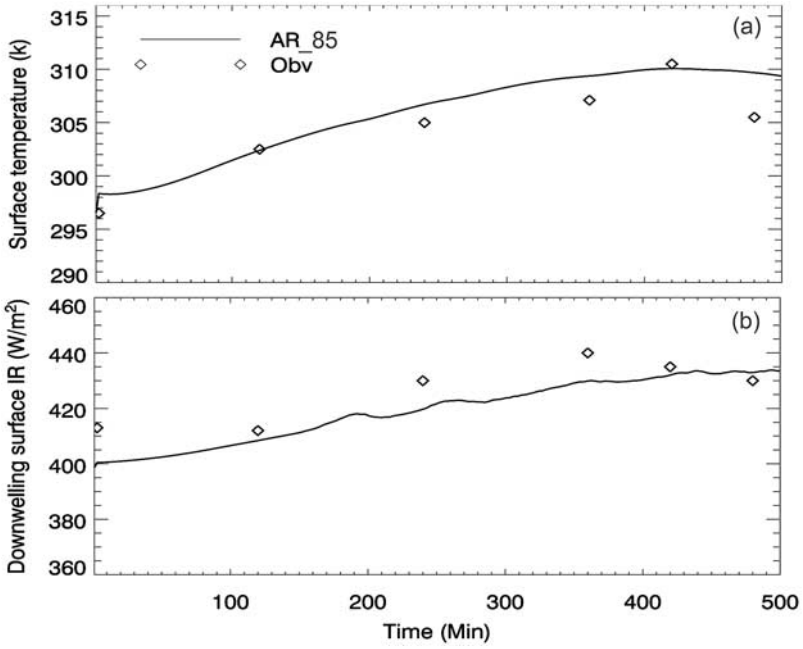


**Figure 2.** Time series of (a) the surface temperature and (b) the downwelling surface infrared fluxes from model simulation AR_85 (solid line) and observations (diamond).

other two calculations with SSA = 0.90 and 0.95 have the similar configurations as AR_85, with the exception of different mixing ratios of BC to ammonium sulfate. The initial mid-visible AOD decreases gradually from 0.27 to 0.25, as SSA increases from 0.85 to 1.0.

[21] All simulations are performed for a 10-h daytime from 7:00–17:00. The analyses of most cloud properties are from 120–480 min because the first 2-hr is considered as the model spin-up time and the strongest convections with the peak ice particle formation occur within one hour before 480 min (the cloud appears to be dissipating after 480 min). In addition, the time period of 120–480 min corresponds to the local time of 9:00–15:00, when the solar radiation is strongest and aerosol radiative effects are more prominent. However, the estimates of forcing are based on the entire daytime simulations.

### 3.2. Validation of the Coupled GCE Model

[22] Although the surface model PLACE and the Goddard radiation scheme have been validated separately in previously studies [*Mohr et al.*, 2003; *Alonge et al.*, 2007; *Tao et al.*, 2003b], the performance of the fully coupled model system is examined here by comparing with observations and other modeling results. Figure 2 shows the comparisons of the surface temperature and the downwelling surface infrared fluxes between the modeled values from AR_85 and the observed values from the site of La Porte in Houston [*Zamora et al.*, 2003, 2005]. The modeled surface temperature and the downwelling surface infrared fluxes are generally in agreement with the observations, although the model tends to slightly overestimate the surface temperature and underestimate the downwelling surface infrared fluxes. The sharp decrease in the observed temperature at 480 min is attributed to a storm occurring at that site. The maximum difference in the downwelling surface infrared fluxes between the modeled and observed values is only about 10 W $m^{-2}$. Because of the poor data quality of the sensible and latent heat fluxes from observations, comparisons of those parameters with the values from the MM5 simulations in the study of surface heat fluxes [*Zamora et al.*, 2003] are provided. The modeled maximum sensible and latent heat fluxes from AR_85 are about 314 and 318 W $m^{-2}$, occurring at 330 and 250 min, respectively, consistent with 310 and 300 W $m^{-2}$ at 360 and 300 min, respectively, from the MM5 simulations. Also, the modeled maximum surface solar flux is 945 W $m^{-2}$, consistent with the observed value of 960 W $m^{-2}$. The good agreement of these parameters between the observations and simulations indicates that the surface model responds correctly to the changes in net radiation and the coupled system is able to provide robust simulations. The overestimation of surface temperature and the earlier peak for heat fluxes have also been observed in other model studies with PLACE [*Mohr et al.*, 2003; *Alonge et al.*, 2007].

[23] In addition, the simulated cloud optical depth ($\tau_c$) is compared with the observed $\tau_c$ from MODIS satellite observations for deep convective clouds in the area. By averaging the $\tau_c$ values from 40 to 100 (deep convective clouds), the model yields a value of about 69, close to the observed average value of 73 for the period of August 2002. The analysis of satellite observations indicates that the average $\tau_c$ for deep convective clouds from 2002 to 2006 does not change appreciably.

## 4. Results and Discussion

### 4.1. Aerosol Radiative Effects (ARE)

[24] Comparisons are made between the simulations with (AR_85) and without the ARE (NAR_00). Figure 3 shows the time series of cloud microphysical fields averaged over all cloudy grids from 120 to 480 min. Note that the aerosol composition and initial size distribution are identical for the two simulations. On the basis of the mean values averaged

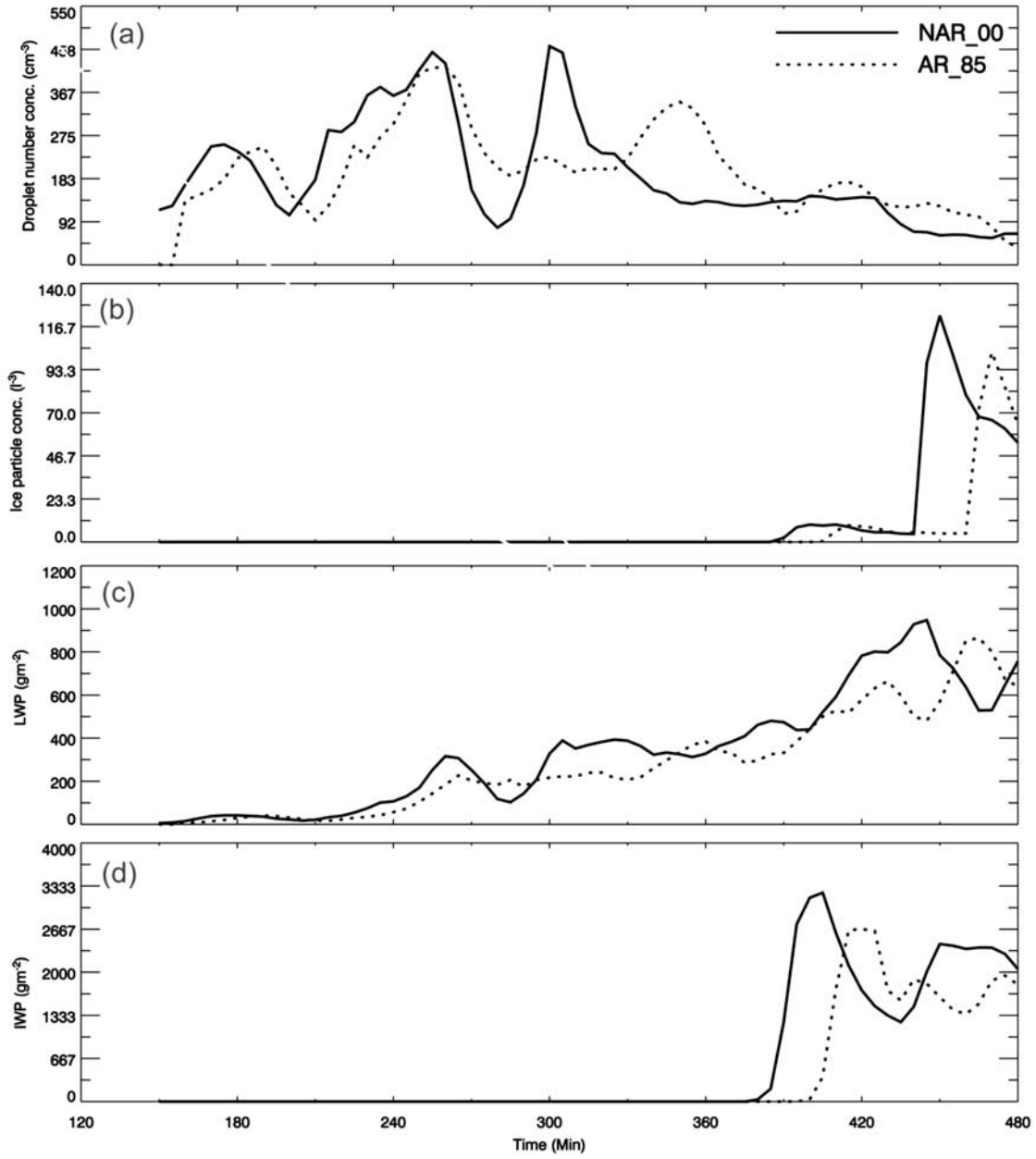


**Figure 3.** Time series of (a) cloud droplet number concentration, (b) ice particle number concentration, (c) LWP, and (d) IWP averaged over all cloudy grids for NAR_00 (solid) and AR_85 (dotted).

over the time period shown in Figure 3a, the droplet number concentration of AR_85 does not differ appreciably from that of NAR_00 (Table 3), since the aerosol composition and size distribution are identical in both cases and the differences in the vertical velocity between the two cases are not large enough to significantly affect the average droplet concentration during the simulation period. However, the simulation with the ARE (AR_85) has much lower ice particle concentrations than that without the ARE (NAR_00) (Figure 3b). The liquid water path (LWP) and ice water path (IWP) for the two cases are presented in Figures 3c and 3d, respectively. The LWP is defined as the sum of the mass-integrated mixing ratios of cloud water and rainwater that determine the water clouds, while IWP is defined as the sum of the mass-integrated mixing ratios of ice crystal, snow, graupel, and hail that determine the ice clouds. With the inclusion of the ARE, both LWP and IWP decrease significantly, by about 15% (Figures 3c and 3d). (Throughout the paper, a claim of significant is based on the average difference over a certain domain and/or time period that is no less than 15%). Also as shown in Figure 3, the peak values of cloud microphysical properties are delayed when the ARE is considered. Ice formation starts at a later time when convection is weak and the cloud does not reach a cold enough temperature. Also, the high ice number concentrations and large IWP occur at different times. At the initial stage of ice clouds, the ice number concentrations are low and ice particles grow quickly, and the cloud area is narrow horizontally but deep vertically, leading to a large average IWP. When the cloud develops to favor ice forma-

**Table 3.** Cloud Properties Averaged Over the Cloudy Grids During 120–480 min for the Simulations NAR_00, AR_85, SA_100, and SAC_100

| Cases | $N_c$, cm$^{-3}$ | $N_i$, L$^{-1}$ | LWP, g m$^{-2}$ | IWP, g m$^{-2}$ | $r_e$, $\mu$m | $\tau_c$[a] | $\tau_c$[b] | $f_{cld}$ | $w_{max}$, m/s | $r_{rain}$[c], mm/h |
|---|---|---|---|---|---|---|---|---|---|---|
| NAR_00 | 191.15 | 34.38 | 335.69 | 1944.99 | 5.85 | 24.34 | 4.83 | 0.18 | 4.98 | 0.18 |
| AR_85 | 203.19 | 22.85 | 286.91 | 1684.01 | 5.59 | 22.41 | 3.83 | 0.15 | 4.56 | 0.09 |
| SA_100 | 253.27 | 31.07 | 337.88 | 1721.31 | 5.50 | 25.64 | 5.06 | 0.18 | 4.82 | 0.18 |
| SAC_100 | 12.98 | 5.11 | 314.34 | 1447.58 | 12.20 | 6.03 | 1.34 | 0.21 | 4.95 | 0.31 |

[a]Cloud optical depth averaged over the cloudy grids during 120–480 min.
[b]Cloud optical depth averaged over the whole horizontal domain and the time period of 120–480 min.
[c]Rain rate averaged over the whole horizontal domain and the time period of 240–480 min, since rain starts around 240 min.

tion later, ice number concentrations are much higher but the cloud is distributed over a larger area to form a thin stratiform cloud, resulting in relatively lower IWP averaged over the cloud area. The mean cloud microphysical properties averaged over the cloudy grids and the simulation time from 120 to 480 min are shown in Table 3. The average cloud droplet number concentration changes from 191 to 203 from NAR_00 to AR_85. This increase is about 5%, which is rather minor. The average ice particle number concentration ($N_i$) in AR_85 is about 35% lower than that in NAR_00. The average LWP and IWP decrease by about 15% when including the ARE, primarily because ARE suppresses convection and results in shallower clouds. The IWP values shown in Table 3 are large because the case simulated represents a deep convective system and there are large amounts of cloud ice, snow, graupel, and hail formation. With the ARE, the average droplet effective radius ($r_e$) is overwhelmingly smaller for AR_85 during the time period of 120–480 min, as shown in Figure 4a: Generally, $r_e$ is about 0.5–1.0 $\mu$m smaller. The average $r_e$ decreases from 5.9 $\mu$m in NAR_00 to 5.6 $\mu$m in AR_85 (Table 3). The vertical profile of $r_e$ (Figure 4b) reveals that the differences in $r_e$ are especially noticeable at heights above 6 km, probably because less water vapor reaches a higher level from a weaker convective strength due to ARE.

[25] The direct radiative effect of strongly absorbing aerosols reduces the incoming solar radiative fluxes at the surface. The reduction in the surface radiative fluxes may lead to a decrease in surface heat fluxes, which suppresses convection. Figure 5 presents the surface temperature and heat fluxes from AR_85 and NAR_00. With the ARE, the average surface temperature decreases by about 0.35 K. The surface sensible heat fluxes decrease by up to 28 W m$^{-2}$, but the latent heat fluxes decrease less significantly than the sensible heat fluxes. The differences in the latent heat fluxes between NAR_00 and AR_85 become smaller starting from 300 min. This is explained since precipitation humidifies the air near the surface in both cases and decreases the latent

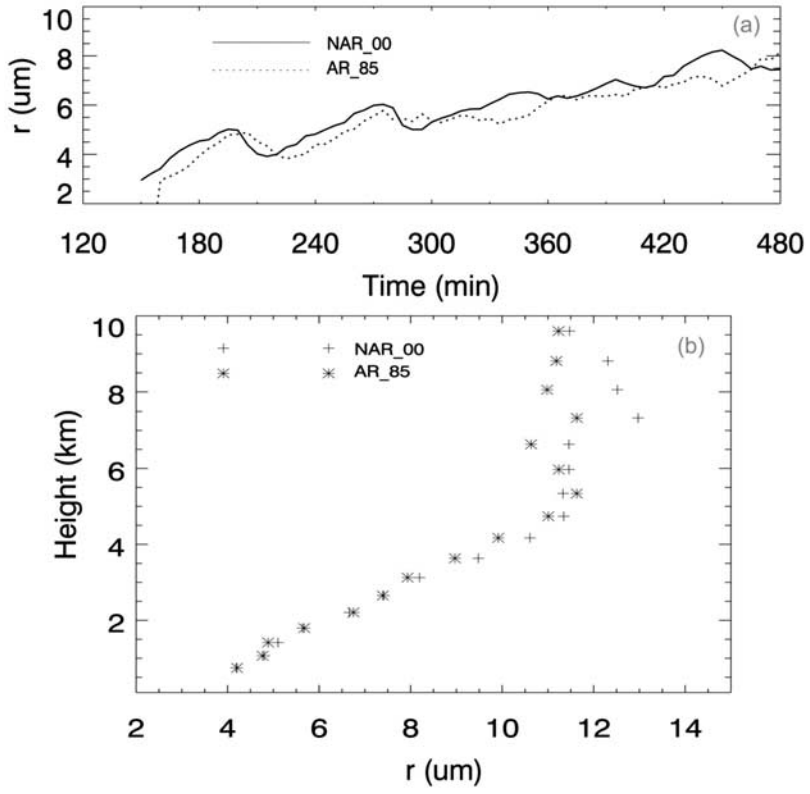


**Figure 4.** (a) Time series of average cloud droplet effective radius ($r_e$), and (b) the vertical profiles of average $r_e$ for NAR_00 and AR_85.

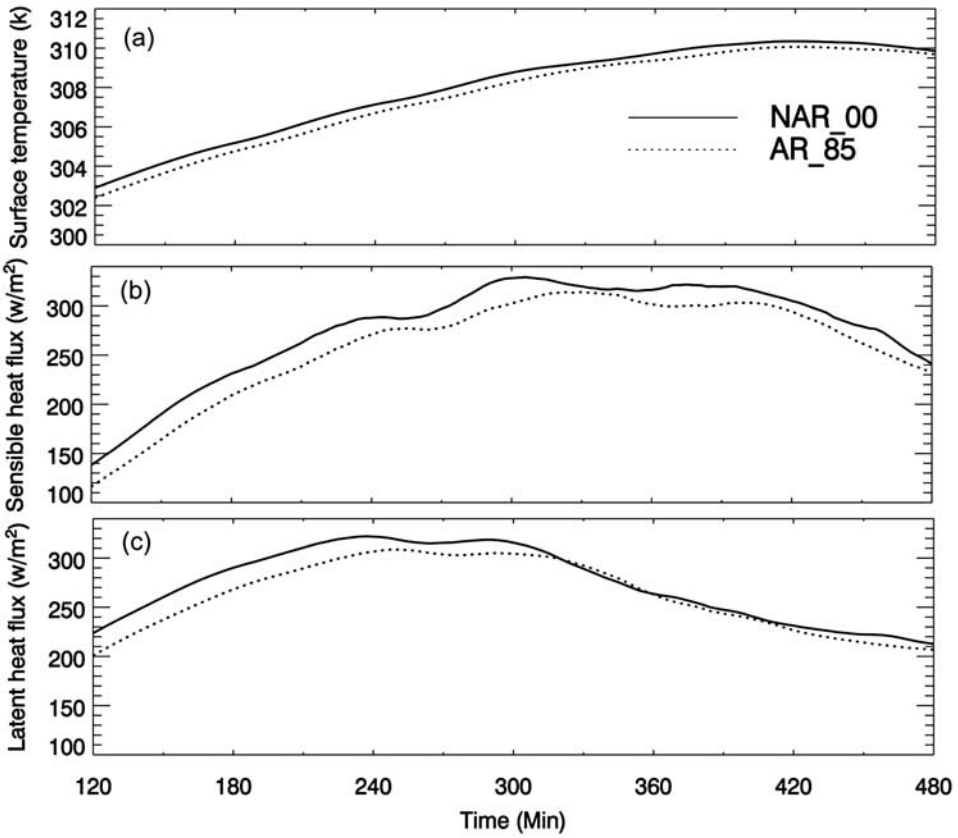


**Figure 5.** Time series of average (a) surface temperature, (b) sensible heat flux, and (c) latent heat flux for NAR_00 and AR_85.

heat fluxes. Figure 6 shows the temporal variation of the updraft velocity averaged over the grids with a velocity greater than 1.0 m/s in the simulation domain. Generally, the convective strength is significantly weaker in AR_85 than that in NAR_00. The averaged domain-maximum updraft velocity ($w_{max}$) during 120–480 min is about 5.0 m/s in NAR_00 and 4.6 m/s in AR_85. Therefore the ARE decreases the surface heat fluxes and weakens the convective strength. The weaker convective strength leads to shallower clouds and weaker ice processes, resulting in less cloudiness, less ice particle concentrations and IWP. Note in Figure 3 and Table 3 the changes in ice microphysical properties are more significantly than those in warm-cloud microphysical properties, because a weaker convection due to ARE leads to less water vapor reaching a higher level, resulting in much weaker ice processes. As shown in Figure 7a, the cloud fractions ($f_{cld}$) over the entire domain in AR_85 (dotted line) are significantly less than those in NAR_00 (solid line). The $f_{cld}$ decreases by about 18% on average (Table 3), with the maximum of over 60% (Figure 7a), when the ARE is considered. The cloud optical depth ($\tau_c$) also decreases significantly (Figure 7b). Averaged over the entire horizontal domain and the time period of 120–480 min, $\tau_c$ decreases by more than 20%, as

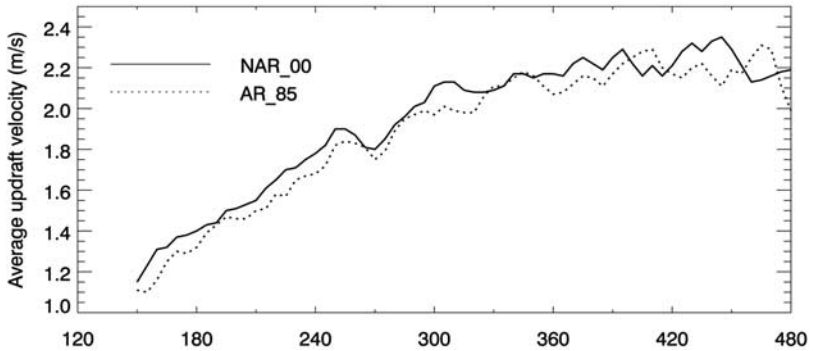


**Figure 6.** Time series of average updraft velocity for NAR_00 and AR_85. The values are averaged over the velocities greater than 1.0 m/s.

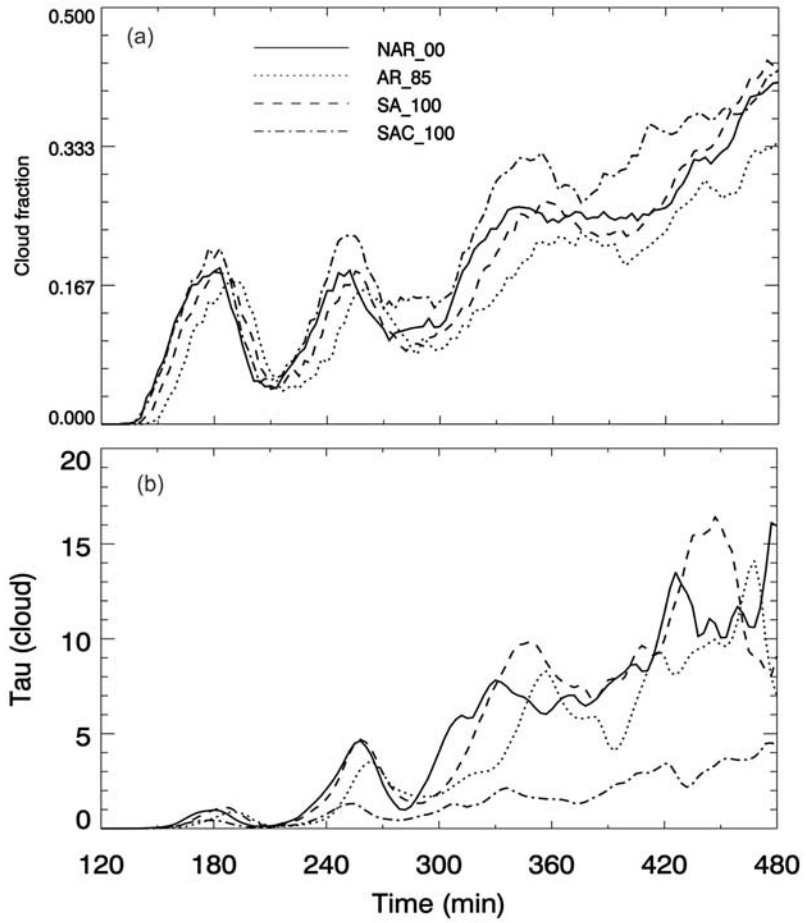


**Figure 7.** Time series of (a) cloud fraction, (b) averaged cloud optical depth over the domain for NAR_00 (solid), AR_85 (dotted), SA_100 (dashed), and SAC_100 (dash-dotted).

shown in Table 3. Note that the magnitude of the averaged $\tau_c$ over the domain is low because of a large domain and low cloud fraction. Also shown in Table 3, the values of $\tau_c$ are much larger when averaged over the cloudy grids. Figure 8 illustrates the vertical profiles of the heating rates averaged over the simulation time of 120–480 min. The heating rates below 5 km in AR_85 are significantly higher than those in NAR_00 due to aerosol absorption. The peak heating rate is at about 2 km with an average value of 2.7 K day$^{-1}$ in AR_85, which is about 0.6 K day$^{-1}$ higher than that in NAR_00. The heating rate of 0.6 K day$^{-1}$ resulting from the aerosol semi-direct effect decreases the relative humidity and temperature lapse rate (Figure 9), contributing to significant decreases in cloud fraction and

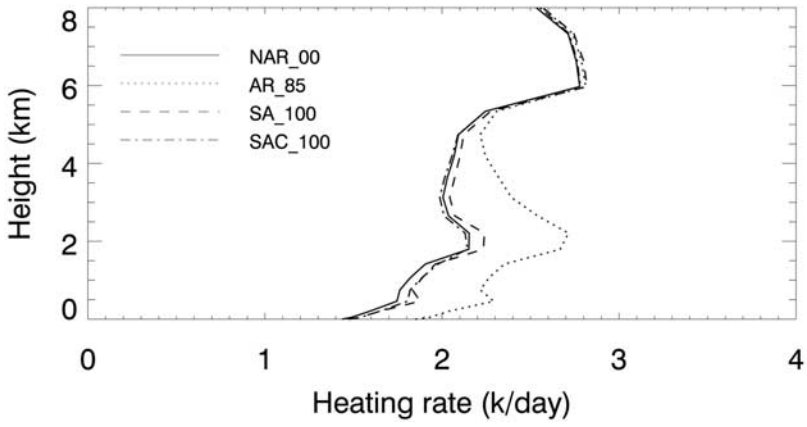


**Figure 8.** Vertical profiles of the heating rates averaged over the horizontal domain for NAR_00, AR_85, SA_100, and SAC_100.

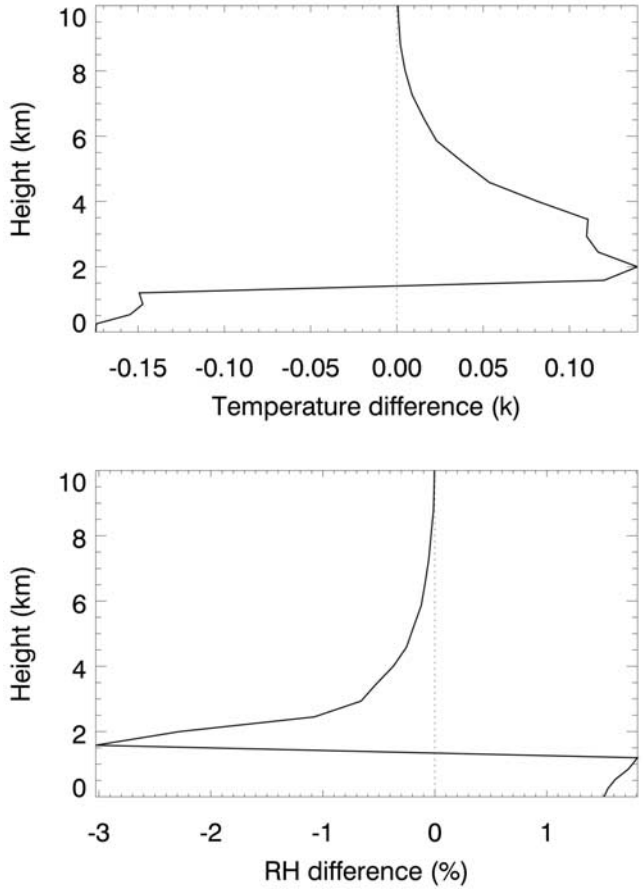


**Figure 9.** Differences in the vertical profiles of (a) temperature and (b) relative humidity between the cases with ARE (AR_85) and without ARE (NAR_00).

cloud optical depth as shown in Figure 7. The decreases in LWP, cloud fraction, and cloud optical depth by including the ARE have also been found by *Jiang and Feingold* [2006] for warm convective clouds.

[26] The differences in the vertical profiles of temperature and relative humidity between the cases with ARE (AR_85) and without ARE (NAR_00) are shown in Figure 9. The data are averaged over the entire domain and the time steps within one hour prior to the cloud formation. With the ARE, the temperature decreases below about 1.6 km above the surface, but increase for the layers above 1.6 km (Figure 9a), indicating a cooling effect near the surface and a heating effect in the elevated atmosphere. The cooling causes an increase of relative humidity near the surface, but the heating decreases the relative humidity significantly aloft (Figure 9b). The heating effect also decreases the temperature lapse rate above the boundary layer, leading to a more stable atmosphere. In order to determine the contribution of the decreased relative humidity and temperature lapse rate to the convection, the differences in CAPE due to the changes in the profiles of temperature ($\Delta CAPE_T$) and relative humidity ($\Delta CAPE_W$) resulting from the ARE are calculated. The results show that $\Delta CAPE_T$ is much more negative than $\Delta CAPE_W$, indicating that the decrease in the temperature lapse rate from the aerosol semi-direct effect may contribute more significantly to the suppression of convection.

[27] The aerosol radiative effects also impact precipitation. The domain-averaged rain rate ($r_{rain}$) during 240–480 min is reduced by about 50% (Table 3). The rain rates are averaged from 240 min when the rain starts. The time dependence of the accumulated rain per grid for NAR_00 (solid line) and AR_85 (dotted line) is shown in Figure 10. With the ARE (AR_85), the accumulated rain also decreases by a factor of 2. The decrease in precipitation primarily results from the shallower clouds due to weaker convection caused by the aerosol radiative effect.

[28] The aerosol radiative effects are further evaluated by comparing the simulations of SA_100 and SAC_100 with the background aerosols (ammonium sulfate only) for the polluted and clean conditions, respectively. Without the absorbing component of aerosols, the cloud fraction and cloud optical depth shown in Figure 7 for SA_100 are close to those for NAR_00, but significantly higher than those for

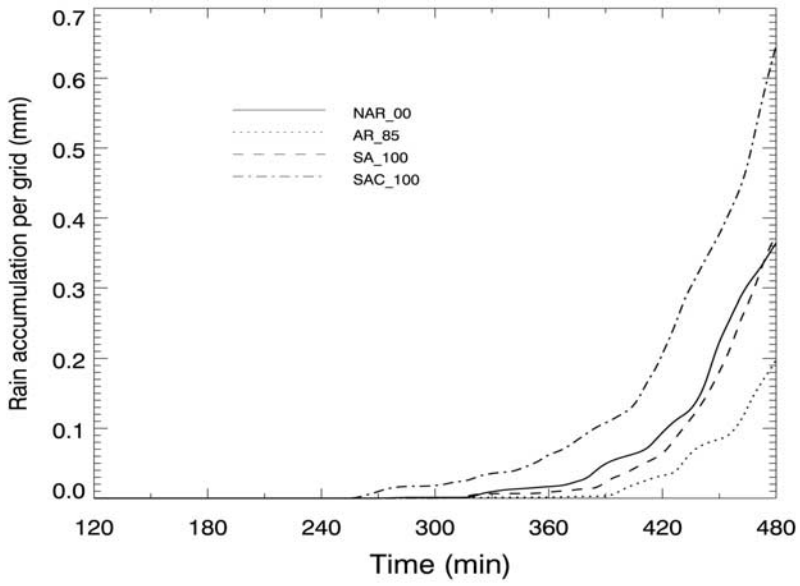


**Figure 10.** Time series of the accumulation rain per grid for NAR_00, AR_85, SA_100, and SAC_100.

**Table 4.** Estimates of Radiative Forcing for AR_85

| W m$^{-2}$ | TOA | SFC |
|---|---|---|
| $f_{\text{total}}$ | −11.6 | −31.9 |
| $f_{\text{direct+semi}}$ | 12.2 | −6.2 |
| $f_{\text{direct}}$ | 2.2 | −17.4 |
| $f_{\text{semi}}$ | 10.0 | 11.2 |
| $f_{\text{indirect}}$ | −23.8 | −25.7 |

AR_85. The clean case (SAC_100) has the largest cloud cover and lowest cloud optical depth, because of much more convective cells and much larger droplet sizes (Figure 7 and Table 3). The simulations without the absorbing component of aerosols (i.e., SA_100 and SAC_100) have the similar vertical profiles of the heating rates as the simulation without the ARE (NAR_00), as shown in Figure 8. The difference in the average surface temperature between the SA_100 and NAR_00 is about 0.25 K, and the differences in the sensible and latent heat fluxes are only a few W m$^{-2}$. Therefore the scattering effect of ammonium sulfate on surface heat fluxes is small. Also as shown in Table 3, SA_100 has a higher cloud droplet number concentration (253.3 cm$^{-3}$) than NAR_00 (191.2 cm$^{-3}$), resulting from the CCN activation processes. The higher droplet number concentrations are responsible for the smaller droplet size in SA_100. Compared with three polluted cases (NAR_00, AR_85, and SA_100), the ice particle number concentrations and IWP in SAC_100 are much lower, indicating a weaker ice process in the clean case due to much less droplet number concentrations and much stronger warm rain processes (coalescence). Figure 10 shows much more precipitation for the clean case than for the polluted cases. In contrast to the increases in convection and precipitation with aerosols in our previous study of aerosol indirect effects on a warm-bubble initiated cumulus cloud [*Fan et al.*, 2007b], the convection and precipitation are suppressed by aerosols for the clouds induced by the surface heating through radiation, when considering the fully interactive radiation and land surface processes. Our results are consistent with the study using a fully coupled cloud-resolving model and land-surface model by *Jiang and Feingold* [2006] for warm convective clouds. The suppressed convection due to aerosol radiative effect was also discussed by *Leaitch et al.* [1983].

[29] Separate estimates of the direct, semi-direct, and indirect forcing values at the TOA and surface (SFC) are made according to the definitions by *McFarquhar and Wang* [2006]. The total forcing ($f_{total}$) is the difference in the net radiative fluxes between the simulation for the polluted air with BC (AR_85) and the simulation with the clean background aerosols (SAC_100). The combination of the direct and semi-direct forcing, $f_{direct+semi}$, is defined as the difference in the net fluxes between the simulation for the polluted air with BC (AR_85) and the simulation with the polluted background aerosols (SA_100), accounting for the direct effect of black carbon on the radiative budget. The difference in the net fluxes between the simulation with the polluted background aerosols (SA_100) and the simulation with the clean background aerosols (SAC_100) corresponds to the non-absorbing aerosol indirect forcing ($f_{indirect}$). The direct forcing of BC, $f_{direct}$, is derived from the difference in the clear-sky net fluxes between the simulations of the polluted air with BC (AR_85) and the polluted background aerosols (SA). Table 4 summarizes the calculated forcing values for AR_85 averaged over the entire domain and during the daytime (from 7:00 to 17:00 local time). The total aerosol radiative forcing, $f_{total}$, at the TOA and surface are −11.6 and −31.9 W m$^{-2}$, respectively. The predicted forcing value at the surface agrees with the observations, about (−30.0) to (−40.0) W m$^{-2}$ [*Fast et al.*, 2006]. The semi-direct forcing of BC, $f_{semi}$, is 10.0 W m$^{-2}$ at the TOA and 11.2 W m$^{-2}$ at the surface. The direct forcing induced by BC is positive (2.2 W m$^{-2}$) at the TOA, but is strongly negative at the surface (−17.4 W m$^{-2}$). The sum of direct and semi-direct forcing, $f_{direct+semi}$, warms the TOA by 12.2 W m$^{-2}$ and cools the surface by a smaller magnitude (−6.2 W m$^{-2}$). Because the semi-direct forcing compensates the direct forcing at the surface, the reduction of the surface fluxes due to the ARE is not so significant, as shown in Figure 5. Compared with the semi-direct forcing estimates of 15 W m$^{-2}$ for stratocumulus by *Johnson et al.* [2004] and of 7.5 W m$^{-2}$ for the trade cumulus by *Ackerman et al.* [2000] at the surface, the estimate of 11.2 W m$^{-2}$ in the present work is close to the median value between the previous studies. *Xu et al.* [2003] reported a daily mean surface direct radiative forcing of −11.2 W m$^{-2}$ over Yangtze delta region in China, slightly higher than our daily mean value of −8.7 W m$^{-2}$ estimated from the daytime-mean value of −17.4 W m$^{-2}$ because of a larger AOD. The TOA indirect radiative forcing ($f_{indirect}$) is estimated to be −23.8 W m$^{-2}$ and the surface $f_{indirect}$ is about −25.7 W m$^{-2}$, much higher than those reported over the tropical Indian Ocean (INDOEX) [*Ramanathan et al.*, 2001b]. For much more polluted air in Houston, the aerosol indirect forcing should be higher than that for the INDOEX case.

### 4.2. Sensitivity to SSA

[30] Table 5 shows the TOA and surface solar radiative fluxes averaged over the entire domain and during the daytime for the simulations with different SSA and the relative net fluxes to the pure ammonium sulfate case (i.e., SSA = 1.0). At the TOA, the upwelling fluxes ($F^{\uparrow}$(TOA))

**Table 5.** Solar Radiative Fluxes for Different SSA and Relative Forcing to Pure Ammonium Sulfate (SSA = 1.0)

| | | | | | | | Net Fluxes Relative to SSA = 1.0 | |
|---|---|---|---|---|---|---|---|---|
| SSA | $F^{\downarrow}$(TOA) | $F^{\uparrow}$(TOA) | $F^{\downarrow}$(SFC) | $F^{\uparrow}$(SFC) | $F_{net}$ (TOA) | $F_{net}$ (SFC) | TOA | SFC |
| 0.85 | 986.81 | −106.62 | 657.15 | −7.57 | 880.18 | 649.58 | 14.05 | −5.81 |
| 0.90 | 986.81 | −112.81 | 658.24 | −7.40 | 874.00 | 650.85 | 7.86 | −4.55 |
| 0.95 | 986.81 | −119.15 | 659.02 | −7.31 | 867.66 | 651.71 | 1.53 | −3.68 |
| 1.00 | 986.81 | −120.67 | 662.62 | −7.23 | 866.13 | 655.39 | 0.00 | 0.00 |

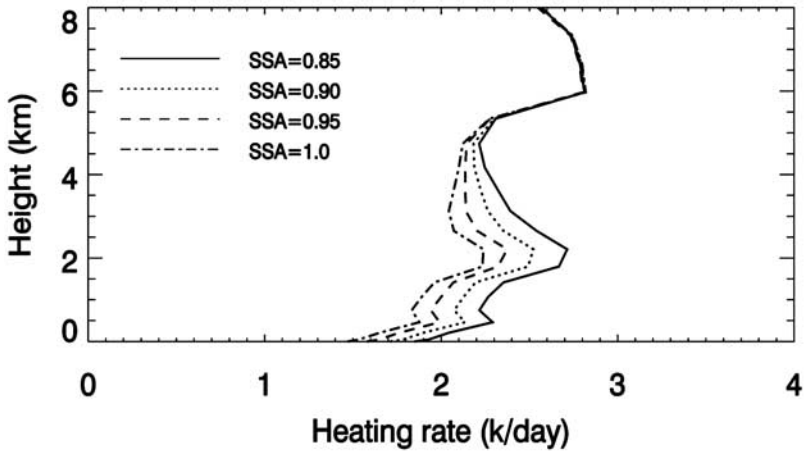


**Figure 11.** Vertical profiles of the heating rates averaged over the horizontal domain for SSA of 0.85 (solid), 0.90 (dotted), 0.95 (dashed), and 1.00 (dash-dotted).

are reduced with the decrease of SSA due to the increase of aerosol absorption, leading to an increase in the net solar radiative fluxes ($F_{net}$(TOA)). The net TOA solar radiative flux increases by 14.05 W m$^{-2}$ when SSA decreases from 1.0 to 0.85, while the net surface solar radiative flux decreases by 5.81 W m$^{-2}$ because of the decrease of the downwelling radiative flux ($F^{\downarrow}$(SFC)) due to the increase of absorption (Table 5). Increasing aerosol absorption leads to higher heating rates in the lower troposphere (Figure 11). The heating rate at 2 km for SSA = 0.85 is about 0.5 K day$^{-1}$ higher than that for SSA = 1.0. At the surface, the heating rate for SSA = 0.85 is also about 0.3 K day$^{-1}$ higher. This surface heating compensates the negative direct forcing, causing the surface temperature to be insensitive to SSA. As shown in Table 6, the average surface temperature ($T_{sfc}$) decreases slightly from 306.09 to 305.98 K as SSA decreases from 1.0 to 0.85. Consequently, the decreases in the surface sensible ($F_{SH}$) and latent heat fluxes ($F_{LH}$) with the decrease of SSA are insignificant (Table 6). *Huang et al.* [2007] also found that the surface temperature did not change considerably because of the canceling effect of semi-direct forcing, consistent with the results in the present study.

[31] Figure 12 illustrates the aerosol radiative forcing versus SSA at the TOA (Figure 12a) and surface (Figure 12b). All the forcing values correspond to the daytime-means. Aerosol absorption is responsible for significant positive direct and semi-direct radiative forcing at the TOA, and the semi-direct effect overwhelms the direct effect for moderately or strongly absorbing aerosol mixtures (Figure 12a). The sum of the direct and semi-direct forcing yields only about 0.6 W m$^{-2}$ positive TOA forcing at SSA = 0.95, but the value increases to 12.1 W m$^{-2}$ at SSA = 0.85. The TOA total radiative forcing values are strongly nega-tive for all SSA cases due to the aerosol indirect effect (Figure 12a). The indirect effect related to the increase in cloud albedo and subsequently negative TOA forcing dominates the positive TOA direct and semi-direct forcing above the clouds for this case. This is in agreement with the inves-tigation by *Keil and Haywood* [2003] of the radiative forcing of biomass-burning aerosols in Southern African. Also seen from Figure 12a, there is significantly less negative TOA forcing with the decrease of SSA due to the absorption of aerosols induced by BC (semi-direct effect).

[32] At the surface, BC leads to strongly negative direct forcing and the value is up to 17.4 W m$^{-2}$ at SSA = 0.85 (Figure 12b). However, the positive semi-direct forcing partially compensates the negative direct forcing. Thus the sum of direct and semi-direct forcing is much less negative, with a value of −6.2 W m$^{-2}$ at SSA = 0.85. *Johnson et al.* [2004] indicated that for marine stratocumulus the semi-direct forcing may well exceed the direct forcing even for moderately absorbing aerosols. Both direct and semi-direct effects are very sensitive to SSA at the surface. Note that aerosol indirect forcing is dominant for the deep convective clouds. Therefore the surface total radiative forcing is much more negative by including the indirect effects, but it is not as sensitive to SSA as the TOA total forcing, due to the compensation of positive semi-direct forcing. The more strongly negative surface radiative forcing for the lower SSA cools the surface and decreases the sensible and latent heat fluxes, leading to weaker convection, less cloudiness and hence lower cloud albedo. These effects are enhanced by the semi-direct effect of absorbing aerosols, which decreases the temperature lapse rate and reduces the relative

**Table 6.** Cloud and Surface Fields for Different SSA

| SSA | $\tau_c$[a] | $f_{cld}$ | $w_{max}$, m/s | Accum. Rain Per Grid, mm[b] | $T_{sfc}$, K | $F_{SH}$, W m$^{-2}$ | $F_{LH}$, W m$^{-2}$ |
|---|---|---|---|---|---|---|---|
| 0.85 | 3.83 | 0.15 | 4.56 | 0.19 | 305.98 | 207.67 | 233.48 |
| 0.90 | 4.15 | 0.16 | 4.62 | 0.28 | 306.03 | 210.88 | 234.57 |
| 0.95 | 4.45 | 0.17 | 4.81 | 0.34 | 306.06 | 212.74 | 235.27 |
| 1.00 | 5.06 | 0.18 | 4.82 | 0.37 | 306.09 | 213.88 | 235.72 |

[a]Cloud optical depth averaged over the whole horizontal domain and the time period of 120–480 min.
[b]The accumulated rain per grid at 480 min.

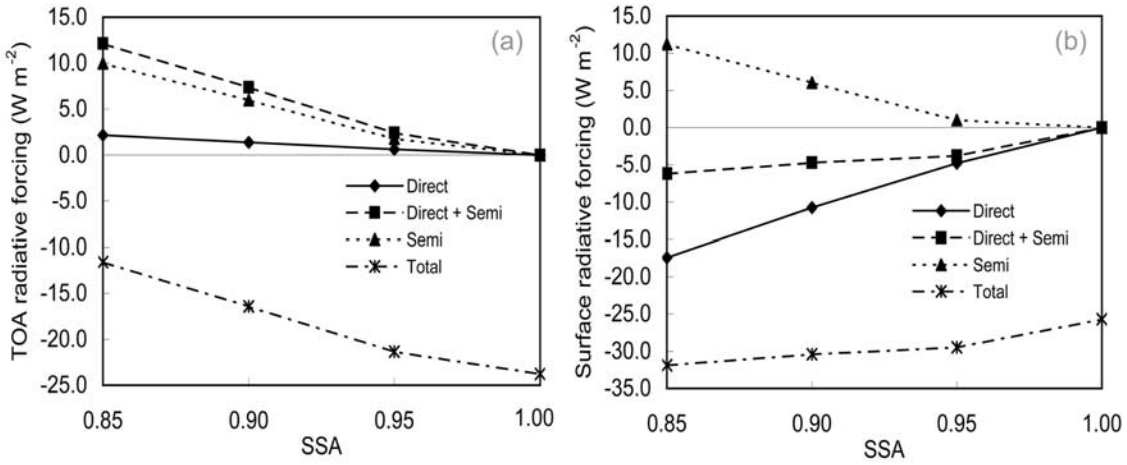


**Figure 12.** The aerosol raidative forcing versus SSA at the (a) TOA and (b) surface.

humidity above the boundary layer, leading to a more stable atmosphere. As shown in Table 6, the averaged domain-maximum updraft velocity during 120–480 min decreases from 4.82 m/s to 4.56 m/s, and the cloud fraction decreases from 0.18 to 0.15 with the decrease of SSA from 1.0 to 0.85. The peak updraft velocity during the entire simulation decreases significantly from 18 m/s for SSA of 1.0 to 13 m/s for SSA of 0.85. The domain-averaged cloud optical depth decreases from 5.06 at SSA = 1.0 to 3.83 at SSA = 0.85.

[33] As demonstrated in section 4.1, the aerosol radiative effects reduce the precipitation. With the increase of absorption (i.e., decrease of SSA), the accumulated rain per grid at 480 min decreases significantly (Table 6). The reduction in precipitation with the decrease of SSA is likely caused by the increase in thermal stability from the BC-induced surface cooling and atmospheric heating, which suppresses convection and inhibits cloud formation. The suppressed precipitation has also been found in a study over the east of Asia on the radiative effect of core-coated internally mixed aerosols containing BC [*Huang et al.*, 2007].

## 5. Conclusion

[34] A spectral-bin cloud-resolving GCE model coupled with a Goddard radiation scheme and an explicit land surface model has been employed to investigate the radiative effects of core-coated internally mixed aerosols containing BC on the deep convective clouds. An aerosol radiative module has been developed to calculate the wavelength-dependent aerosol radiative properties on the basis of the aerosol composition, size distribution, mixing state, and ambient relative humidity. The sensitivity of cloud properties and the associated radiative forcing to aerosol single-scattering albedo (SSA) have also been examined.

[35] Aerosol radiative effects on cloud properties are pronounced for mid-visible SSA of 0.85. Relative to the case excluding the ARE, cloud fraction and optical depth decrease by about 18% and 20%, respectively. Ice particle number concentrations, LWP, IWP, and droplet size decrease by more than 15% when the ARE is introduced. The ARE causes a surface cooling of about 0.35 K and significantly high heating rates in the lower troposphere (about 0.6 K $day^{-1}$ higher at 2 km), both of which lead to a more stable atmosphere and hence weaker convection. The semi-direct effect of aerosols decreases the temperature lapse rate and reduces the relative humidity above the boundary layer and, consequently, suppresses convection. The weaker convection explains the less cloudiness, lower cloud optical depth, less LWP and IWP, smaller droplet size, and less precipitation resulting from the ARE. The ice microphysical properties change more significantly than warm-cloud microphysical properties, because the weaker convection due to ARE leads to less water vapor reaching a higher level, resulting in much weaker ice processes. The daytime-mean direct forcing induced by black carbon is about 2.2 W $m^{-2}$ at the TOA and $-17.4$ W $m^{-2}$ at the surface for SSA = 0.85. The positive semi-direct forcing of 11.2 W $m^{-2}$ compensates the negative direct forcing at the surface, causing a much less negative forcing. Both the TOA and surface total radiative forcing values are strongly negative for the deep convective clouds, about $-11.6$ and $-31.9$ W $m^{-2}$, respectively, attributed mostly to the aerosol indirect forcing.

[36] Aerosol direct and semi-direct effects are very sensitive to SSA when aerosol optical depth is relatively high. The TOA semi-direct forcing increases significantly with the decrease of SSA by decreasing the upwelling radiative fluxes due to the increase of aerosol absorption. At the surface, decreasing SSA (increasing absorption) leads to a significant reduction of direct forcing, and a significant increase of semi-direct forcing. Because the positive semi-direct forcing compensates the negative direct forcing at the surface, the surface temperature and heat fluxes decrease less significantly. The aerosol indirect forcing is dominant for deep convective clouds. The cloud fraction, optical depth, convective strength, and precipitation decrease with increasing absorption, resultant from a more stable atmosphere due to enhanced surface cooling and atmospheric heating.

[37] Our studies reveal that the direct and indirect aerosol effects on clouds and precipitation are strongly dependent on aerosol properties, cloud thermodynamic and microphysical conditions, and the interacting processes. In our previous work of a cumulus cloud initiated by a warm bubble

and with a prescribed surface fluxes, the aerosol indirect effects led to stronger convection, larger cloud coverage, and enhanced precipitation without considering radiation and surface processes [*Fan et al.*, 2007a, 2007b]. However, for absorbing aerosols and clouds induced by surface heat fluxes through radiation with the consideration of fully interactive land surface and radiation processes, aerosol radiative effects appear to more significant, by suppressing convection and leading to less cloud fraction, lower cloud optical depth, and less precipitation. The aerosol radiative effects result in about 20% differences in cloud statistical characteristics and 50% on precipitation. Those are significant results and are unlikely attributable to the numerical uncertainties (such as noise or other artificial factors). The presently numerical scheme used in the GCE model corresponds to a state-of-the-art Multidimensional Positive Definite Advection Transport Algorithm (MPDATA), which generally produces less numerical noise [*Johnson et al.*, 2004]. Also, our results are consistent with the previously published work that uses a fully coupled cloud-resolving model and land-surface model by *Jiang and Feingold* [2006].

[38] The present results show that aerosols with moderate or strong absorption heat the lower atmosphere significantly, change the energy balance between the surface and the atmosphere, and stabilize the atmosphere. The reduction in cloud fraction by absorbing aerosols may represent one of the mechanisms contributing to the global warming despite the aerosol cooling effect. In addition, this study implies that the smoky aerosols from biomass burning may suppress convections and reduce the precipitation, modifying the water cycle and impacting the climate.

[39] **Acknowledgments.** This study was supported by NSF (ATM-0424885). J. Fan was supported by NASA Headquarters under the Earth System Science (ESS) Fellowship. The GCE model is mainly supported by the NASA Headquarters Atmospheric Dynamics and Thermodynamics Program and the NASA TRMM. W.-K. Tao is grateful to R. Kakar at NASA headquarters for his support. W.-K. Tao was supported by the Office of Science (BER), U. S. Department of Energy/Atmospheric Radiation Measurement (DOE/ARM) Interagency Agreement No. DE-AI02-04ER63755. W.-K. Tao is grateful to Kiran Alapaty at DOE/ARM for his support. A. Khain of HUJI is acknowledged for the use of the spectral-bin microphysics code. The authors also thank Jerome Fast of PNNL for providing observed aerosol optical data, and Robert J. Zamora of NOAA for providing the observed surface data. Tianle Yuan of UMD is thanked for the satellite observations of cloud optical depth.

## References

Ackerman, T. P., and O. B. Toon (1981), Absorption of visible radiation in atmosphere containing mixtures of absorbing and non-absorbing particles, *Appl. Opt.*, *20*, 3661–3667.

Ackerman, A. S., et al. (2000), Reduction of tropical cloudiness by soot, *Science*, *288*, 1042–1047.

Alonge, C. J., K. I. Mohr, and W.-K. Tao (2007), Numerical case studies of wet vs. dry regimes in the West African Sahel, *J. Hydrometeorol.*, *8*, 102–116.

Baker, R. D., B. H. Lynn, A. Boone, W.-K. Tao, and J. Simpson (2001), The influence of soil moisture, coastline curvature, and land-breeze circulations on sea-breeze initiated precipitation, *J. Hydrometeorol.*, *2*, 193–211.

Bohren, C. F., and D. R. Huffman (1983), *Absorption and Scattering of Light by Small Particles*, John Wiley & Sons, New York.

Bond, D. W., R. Zhang, X. Tie, G. Brasseur, G. Huffines, R. E. Orville, and D. J. Boccippio (2001), $NO_x$ production by lightning over the continental United States, *J. Geophys. Res.*, *106*, 27,701–27,709.

Brock, C. A., et al. (2003), Particle growth in urban and industrial plumes in Texas, *J. Geophys. Res.*, *108*(D3), 4111, doi:10.1029/2002JD002746.

Businger, J. A., J. C. Wyngaard, Y. Izumi, and E. F. Bradley (1971), Flux-profile relationships in the atmospheric surface layer, *J. Atmos. Sci.*, *28*, 181–189.

Charlson, R. J., and M. J. Pilat (1969), Climate: The influence of aerosols, *J. Appl. Meteorol.*, *8*, 1001–1002.

Chazette, P., and C. Liousse (2001), A case study of optical and chemical ground apportionment for urban aerosols in Thessaloniki, *Atmos. Environ.*, *35*, 2497–2506.

Chou, M.-D., and M. J. Suarez (1999), A shortwave radiation parameterization for atmospheric studies, *15, NASA/TM-104606*, p. 40.

Chou, M.-D., K.-T. Lee, S.-C. Tsay, and Q. Fu (1999), Parameterization for cloud longwave scattering for use in atmospheric models, *J. Clim.*, *12*, 159–169.

Chylek, P., G. Videen, D. Ngo, R. G. Pinnick, and J. D. Klett (1995), Effect of black carbon on the optical properties and climate forcing of sulfate aerosols, *J. Geophys. Res.*, *100*, 16,325–16,332.

Coakley, J. A., Jr., R. D. Cess, and F. B. Yurevich (1983), The effect of tropospheric aerosols on the earth's radiation budget: A parameterization for climate models, *J. Atmos. Sci.*, *40*, 116–138.

Fan, J., R. Zhang, G. Li, J. Nielsen-Gammon, and Z. Li (2005), Simulations of fine particulate matter ($PM_{2.5}$) in Houston, Texas, *J. Geophys. Res.*, *110*, D16203, doi:10.1029/2005JD005805.

Fan, J., R. Zhang, D. Collins, and G. Li (2006), Contribution of secondary condensable organics to new particle formation: A case study in Houston, Texas, *Geophys. Res. Lett.*, *33*, L15802, doi:10.1029/2006GL026295.

Fan, J., R. Zhang, G. Li, W.-K. Tao, and X. Li (2007a), Simulations of cumulus clouds using a spectral microphysics cloud-resolving model, *J. Geophys. Res.*, *112*, D04201, doi:10.1029/2006JD007688.

Fan, J., R. Zhang, G. Li, and W.-K. Tao (2007b), Effects of aerosols and relative humidity on cumulus clouds, *J. Geophys. Res.*, *112*, D14204, doi:10.1029/2006JD008136.

Fast, J. D., W. I. Gustafson Jr., R. C. Easter, R. A. Zaveri, J. C. Barnard, E. G. Chapman, G. A. Grell, and S. E. Peckham (2006), Evolution of ozone, particulates, and aerosol direct radiative forcing in the vicinity of Houston using a fully coupled meteorology-chemistry-aerosol model, *J. Geophys. Res.*, *111*, D21305, doi:10.1029/2005JD006721.

Feingold, G., H. Jiang, and J. Y. Harrington (2005), On smoke suppression of clouds in Amazonia, *Geophys. Res. Lett.*, *32*, L02804, doi:10.1029/2004GL021369.

Hänel, G. (1976), The properties of atmospheric particles as functions of the relative humidity at thermodynamic equilibrium with surrounding moist air, *Adv. Geophys.*, *19*, 73–188.

Hansen, J., M. Sato, and R. Ruedy (1997), Radiative forcing and climate response, *J. Geophys. Res.*, *102*(D6), 6832–6864.

Hegg, A. D., J. Livingston, P. V. Hobbs, T. Novakov, and P. Russell (1997), Chemical apportionment of aerosol column optical depth off the mid-Atlantic coast of the United States, *J. Geophys. Res.*, *102*, 25,293–25,303.

Huang, Y., W. L. Chameides, and R. E. Dickinson (2007), Direct and indirect effects of anthropogenic aerosols on regional precipitation over east Asia, *J. Geophys. Res.*, *112*, D03212, doi:10.1029/2006JD007114.

Intergovernmental Panel on Climate Change (IPCC) (2001), *The Scientific Basis*, Cambridge Univ. Press, New York.

Jacobson, M. Z. (1999), Isolating nitrated and aromatic aerosols and nitrated and aromatic gases as sources of ultraviolet light absorption, *J. Geophys. Res.*, *104*, 3527–3542.

Jiang, H., and G. Feingold (2006), Effect of aerosol on warm convective clouds: Aerosol-cloud-surface flux feedbacks in a new coupled large eddy model, *J. Geophys. Res.*, *111*, D01202, doi:10.1029/2005JD006138.

Johnson, B. T., K. P. Shine, and P. M. Forster (2004), A semi-direct aerosol effect: Impact of absorbing aerosols on marine stratocumulus, *Q. J. R. Meteorol. Soc.*, *130*, 1407–1422.

Keil, A., and J. M. Haywood (2003), Solar radiative forcing by biomass burning aerosol particles during SAFARI 2000: A case study based on measured aerosol and cloud properties, *J. Geophys. Res.*, *108*(D13), 8467, doi:10.1029/2002JD002315.

Khain, A. P., and A. Pokrovsky (2004), Simulation of effects of atmospheric aerosols on deep turbulent convective clouds using a spectral microphysics mixed-phase cumulus cloud model. Part II: Sensitivity study, *J. Atmos. Sci.*, *61*, 2983–3001.

Khain, A. P., A. Pokrovsky, M. Pinsky, A. Seifert, and V. Phillips (2004), Simulation of effects of atmospheric aerosols on deep turbulent convective clouds using a spectral microphysics mixed-phase cumulus cloud model. Part I: Model description and possible applications, *J. Atmos. Sci.*, *61*, 2963–2982.

Khairoutdinov, M. F., and D. A. Randall (2003), Cloud resolving modeling of the ARM summer 1997 IOP: Model formulation, results, uncertainties, and sensitivities, *J. Atmos. Sci.*, *60*, 607–625.

Kratz, D. P., M.-D. Chou, M.-H. Yan, and C.-H. Ho (1998), Minor trace gas radiative forcing calculations using the k-distribution method with one-parameter scaling, *J. Geophy. Res.*, *103*, 31,647–31,656.

Leaitch, W. R., J. W. Strapp, G. A. Isaac, and H. G. Leighton (1983), Radiative effects of large scale haze, 5th Conference on Atmospheric Radiation, American Meteorological Society, Baltimore, MD.

Lei, W., R. Zhang, X. Tie, and P. Hess (2004), Chemical characterization of ozone formation in the Houston-Galveston area, *J. Geophys. Res.*, *109*, D12301, doi:10.1029/2003JD004219.

Levitt, N. P., R. Zhang, H. Xue, and J. Chen (2007), Heterogenous chemistry of organic acids on soot surfaces, *J. Phys. Chem. A*, *111*, 4804–4814.

Li, G., R. Zhang, J. Fan, and X. Tie (2005), Impacts of black carbon aerosol on photolysis and ozone, *J. Geophys. Res.*, *110*, D23206, doi:10.1029/2005JD005898.

Li, G., R. Zhang, J. Fan, and X. Tie (2007), Impacts of biogenic emissions on photochemical ozone production in Houston, Texas, *J. Geophys. Res.*, *112*, D10309, doi:10.1029/2006JD007924.

Lynn, B. H., W.-K. Tao, and P. J. Wetzel (1998), A study of landscape generated deep moist convection, *Mon. Weather Rev.*, *126*, 928–942.

Mallet, M., J. C. Roger, S. Despiau, J. P. Putaud, and O. Dubovik (2004), A study of the mixing state of black carbon in urban zone, *J. Geophys. Res.*, *109*, D04202, doi:10.1029/2003JD003940.

McFarquhar, G. M., and H. Wang (2006), Effects of aerosols on trade wind cumuli over the Indian Ocean: Mosel simulations, *Q. J. R. Meteorol. Soc.*, *132*, 821–843.

Mohr, K. I., R. D. Baker, W.-K. Tao, and J. S. Famiglietti (2003), The sensitivity of West African convection line water budgets to land cover, *J. Hydrometeorol.*, *4*, 62–76.

Orville, R. E., G. Huffines, J. Nielsen-Gammon, R. Zhang, B. Ely, S. Steiger, S. Philips, S. Allen, and W. Read (2001), Enhancement of cloud-to-ground lightning over Houston, Texas, *Geophys. Res. Lett.*, *28*, 2597–2600.

Pruppacher, H. R., and J. D. Klett (1997), *Microphysics of clouds and precipitation*, 2nd ed., p. 914, Oxford Press.

Ramachandran, S. (2005), Aerosol radiative forcing over Bay of Bengal and Chennai: Comparison with maritime, continental, and urban aerosol models, *J. Geophys. Res.*, *110*, D21206, doi:10.1029/2005JD005861.

Ramanathan, V., et al. (2001a), The Indian Experiment: An integrated assessment of the climate forcing and the effects of the great Indo-Asian haze, *J. Geophys. Res.*, *106*, 28,371–28,398.

Ramanathan, V., P. J. Crutzen, J. T. Kiehl, and D. Rosenfeld (2001b), Aerosol, climate and the hydrological cycle, *Science*, *294*, 2119–2124.

Rosenfeld, D. (2000), Suppression of rain and snow by urban and industrial air pollution, *Science*, *287*, 1793–1796.

Tao, W.-K., and J. Simpson (1993), The Goddard Cumulus Ensemble model. Part I: Model description, *Terr. Atmos. Oceanic Sci.*, *4*, 19–54.

Tao, W.-K., et al. (2003a), Microphysics, radiation, and surface processes in the Goddard Cumulus Ensemble (GCE) model, *Meteor. Atmos. Phys.*, *82*, 97–137.

Tao, W.-K., C.-L. Shie, J. Simpson, S. Braun, R. H. Johnson, and P. E. Ciesielski (2003b), Convective systems over the south China sea: Cloud-resolving model simulations, *J. Atmos. Sci.*, *60*, 2929–2956.

Twomey, S. (1977), The influence of pollution on the shortwave albedo of clouds, *J. Atmos. Sci.*, *34*, 1149–1152.

Wang, C. (2004), A modeling study on the climate impacts of black carbon aerosols, *J. Geophys. Res.*, *109*, D03106, doi:10.1029/2003JD004084.

Wetzel, P. J., and A. Boone (1995), A Parameterization for Land-Atmosphere-Cloud Exchange (PLACE), documentation and testing of a detailed process model of the partly cloudy boundary layer over heterogeneous land, *J. Clim.*, *8*, 1810–1837.

Wolf, S. (2002), Mie scattering in particle ensembles under consideration of large size parameter, California Institute of Technology, CA 91125.

Xu, J., M. H. Bergin, R. Greenwald, and P. B. Russell (2003), Direct aerosol radiative forcing in the Yangtze delta region of China: Observation and model estimation, *J. Geophys. Res.*, *108*(D2), 4060, doi:10.1029/2002JD002550.

Zamora, R. J., J. M. Wilczak, J.-W. Bao, and S. A. Michelson (2003), Heat flux and energy balance in Houston, *A progress report to the Technical Analysis Division, Texas Commission on Environmental Quality (TCEQ)*, May 30.

Zamora, R. J., E. G. Dutton, M. Trainer, S. A. McKeen, J. M. Wilczak, and Y.-T. Hou (2005), The accuracy of solar irradiance calculations used in mesoscale numerical weather prediction, *Mon. Weather Rev.*, *133*, 783–792.

Zhang, D., and R. Zhang (2005), Laboratory investigation of heterogeneous interaction of sulfuric acid with soot, *Environ. Sci. Technol.*, *39*, 5722–5727.

Zhang, R., X. Tie, and D. W. Bond (2003), Impacts of anthropogenic and natural $NO_x$ sources over the U.S. on tropospheric chemistry, *Proc. Natl. Acad. Sci. USA*, *100*, 1505–1509.

Zhang, R., I. Suh, J. Zhao, D. Zhang, E. C. Fortner, X. Tie, L. T. Molina, and M. J. Molina (2004a), Atmospheric new particle formation enhanced by organic acids, *Science*, *304*, 1487–1490.

Zhang, R., W. Lei, X. Tie, and P. Hess (2004b), Industrial emissions cause extreme diurnal urban ozone variability, *Proc. Natl. Acad. Sci. USA*, *101*, 6346–6350.

Zhang, R., G. Li, J. Fan, D. L. Wu, E. R. Williams, and M. J. Molina (2007), Intensification of Pacific storm track linked to Asian pollution, *Proc. Natl. Acad. Sci. USA*, *104*, 5295–5299.

Zilitinkevich, S. S. (1975), Comments on "A model for the dynamics of the inversion above a convective boundary layer", *J. Atmos. Sci.*, *32*, 991–992.

J. Fan, Climate Physics, Pacific Northwest National Laboratory, PO Box 999, MSIN k9-24, Richland, WA 99352, USA.

K. I. Mohr, Department of Earth and Atmospheric Sciences, University at Albany, SUNY, Albany, NY 12222, USA.

W.-K. Tao, NASA Goddard Space Flight Center, Code 613.1, Greenbelt, MD 20771, USA.

R. Zhang, Department of Atmospheric Sciences, Texas A&M University, 1204 Eller O&M Building, 3150 TAMU, College Station, TX 77843-3150, USA. (renyi-zhang@neo.tamu.edu)